

Nanostructured porous carbons with high rate cycling and floating performance for supercapacitor application

F. O. Ochai-Ejeh,¹ D. Y. Momodu,¹ M. J. Madito,¹ A. A. Khaleed,¹
K. O. Oyedotun,¹ S. C. Ray,² and N. Manyala^{1,a}

¹Department of Physics, Institute of Applied Materials, SARChI Chair in Carbon Technology and Materials, University of Pretoria, 0028, South Africa

²Department of Physics, University of South Africa, Florida Science Campus, Florida, Johannesburg 1709, South Africa

(Received 20 January 2018; accepted 22 April 2018; published online 8 May 2018)

Biomass-derived activated carbon from cork (*Quercus Suber*) (ACQS) was prepared via a two-step environment-friendly route using mild KHCO_3 as the activating agent. This synthesis route makes the material produced less toxic for usage as electrode material for energy storage application. The ACQS has well-defined microporous and mesoporous structures and a specific surface area of $1056.52 \text{ m}^2 \text{ g}^{-1}$ and pore volume of $0.64 \text{ cm}^3 \text{ g}^{-1}$. Three-electrode tests were performed in 6 M KOH, 1 M H_2SO_4 and 3 M KNO_3 aqueous electrolytes, to analyse the material performance in acidic, basic, and neutral media. Specific capacitance values (C_s) of $133 \text{ F g}^{-1}/167 \text{ F g}^{-1}$ at 1.0 A g^{-1} was obtained in 3 M KNO_3 in the positive/negative potential windows. Due to the observed best performance in neutral 3 M KNO_3 , further electrochemical analysis of the symmetric device was carried out using the same electrolyte. The device displayed a C_s value of 122 F g^{-1} , energy and power densities of $\sim 14 \text{ W h kg}^{-1}$ and 450 W kg^{-1} respectively; at 0.5 A g^{-1} . The device also displayed an excellent stability after potentiostatic floating at a maximum voltage of 1.8 V for 120 h and $\sim 100\%$ capacitance retention after 10,000 charge-discharge cycles. The excellent stability makes the cork-derived material a potential excellent, cost-effective material for supercapacitor application. © 2018 Author(s). All article content, except where otherwise noted, is licensed under a Creative Commons Attribution (CC BY) license (<http://creativecommons.org/licenses/by/4.0/>). <https://doi.org/10.1063/1.5023046>

I. INTRODUCTION

Dependence on the energy supply from limited fossil fuels has led to increased environmental pollution and degradation through the emission of air pollutants and greenhouse gases.¹⁻³ A better way to combat this issue is by designing a means by which the amount of energy produced by fossil fuels is drastically reduced via conversion into cleaner and safer energy generation routes. The realistic solution to a clean, renewable, sustainable, efficient and safer energy generation option is in the use of renewable energy from clean sources such as the sun, wind, geothermal, plant biomass waste amongst others.^{1,4,5} Biomass waste materials have been referred to as one of the key renewable energy sources which transform raw waste into porous carbons for supercapacitor application.^{3,6,7} However, to successfully pilot the as-generated energy for effective use in different applications, there is a need for a reliable and efficient storage model.² The most common storage gadgets today are high-performance batteries (hpBs) which are plagued with low power densities and to some safety issues which limits their use in high-power applications.^{8,9}

^aCorresponding author's email: ncholu.manyala@up.ac.za; Tel.: + (27)12 420 3549; Fax: + (27)12 420 2516



Electrochemical capacitors (ECs) on the other hand, which are characterized by reasonably high power density, good cyclic life, relative high safety and low maintenance cost, have been reported as an emerging storage technology with a potential to replace/compliment batteries even though they are plagued with low energy density as well, as compared to batteries.¹⁰⁻¹³ The backbone behind the excellent performance of both batteries and supercapacitors lie in the nature of the materials used to make up the devices. Therefore, it is highly important to develop highly functional materials that will be able to store energy efficiently over time. ECs make use of different forms of materials as electrode materials. Among these materials, porous carbons have been widely and commercially utilized successfully due to their long-term cycling stability, easy production, ability to operate in aqueous and non-aqueous electrolytes, large specific surface areas (SSA), good conductivity, low cost, nontoxicity and tunable microstructure etc.^{1,4,8,14-17} Owing to these numerous advantages, activated carbon has been employed in different applications such as drug delivery systems, absorbents, hydrogen storage and electrochemical energy storage.^{1,3,18-20}

Numerous studies on the conversion of biomass wastes to materials for various applications have been carried out^{7,18,21-25} using pre-treatment hydrothermal techniques, simple drying, spray drying, pyrolysis, controlled combustion in an inert gas. Studies have shown that for electrochemical energy storage applications, the appropriate combination of micropore/mesopore volume, surface area, and pore size distribution is ideal for excellent supercapacitor performance which combines good specific capacitance value with good rate capability, high rate power delivery, high energy storage capability without compromising the stability.^{1,7,23} To achieve this, strategic physical or chemical processes are required to produce carbons of the desired properties.^{1,7} The physical process involves gasifying carbon precursors previously carbonized in an inert atmosphere with CO₂, O₂ or steam within a temperature range of 600 - 1200 °C, while chemical activation involves impregnating the carbon precursor with activating agents like ZnCl₂, H₂SO₄, KOH, etc. The latter is the most commonly utilized because it results in a material with high specific surface areas and high micropore volume with good pore size distribution which are necessary for good electrochemical performance.^{11,20} Although, KOH has been considered to be corrosive leading to limitation in its industrial utilization,^{23,26} interestingly in our earlier studies⁹ KOH was utilized as an activating agent, and was optimized with respect to KOH - raw material mass ratio, carbonization temperature and time to obtain activated carbon material activated with mild KOH concentration having good microstructures suitable for better electrochemical performance and an environment friendly energy storage device were established.

In this regard, the present study embarked on the use of mild KHCO₃ activating agent (which is even more environmentally friendly as compared to KOH) in a 1:1 ratio with hydrothermally treated active raw cork (*Quercus Suber*) biomass for the material synthesis. An extensive electrochemical testing of the as-synthesized ACQS material was done in the three-electrode set-up in acidic 1 M H₂SO₄, alkaline 6 M KOH and neutral 3 M KNO₃ aqueous electrolytes to obtain the best working parameters in the half-cell electrodes. From the analysis, 3 M KNO₃ neutral electrolyte was then adopted for the design of the full device based on its outstanding performance in both positive and negative potentials. The results obtained show-cased an excellent stability up to 10,000 charge-discharge cycles, excellent capacitance retention and an exceptional capacitance improvement after the first 10 h of the 120 h floating period depicting a relatively stable symmetric device with a potential for energy storage.

II. EXPERIMENTAL DETAILS

A. Material synthesis

10 g of raw cork (*Quercus Suber*) was washed using acetone and deionized water and dried in an oven at 60 °C for several hours. Then the raw cork was pre-treated with 0.8 ml of 0.5 M sulfuric acid and 80 ml deionized water in a hydrothermal system at 160 °C for 12 hours. The hydrochar obtained was washed with deionized water several times and dried in an oven. The hydrochar was then ground and re-weighed and activated with potassium hydrogen carbonate (KHCO₃) in a ratio of 1:1. The activated hydrochar was carbonized under argon flow in a chemical vapour deposition system at

850 °C for 2 hours. The product obtained was then washed several times using 3 M HCl and deionized water and dried in an oven at 60 °C overnight.

B. Material characterization

Scanning electron microscopy (SEM) measurements were performed using Zeiss Ultra plus 55 field emission scanning electron microscope (FE-SEM) operating at an accelerating voltage of 2.0 kV. Energy-dispersive X-ray (EDX) analysis, high-resolution transmission electron microscopy (HRTEM) and selected area diffraction (SAED) analysis of the sample was measured using JEOL 2100 (Tokyo Japan) operated at 200 kV. X-ray photoelectron spectroscopy (XPS) measurements were performed using a Physical Electronics Versa Probe 5000 spectrometer. X-ray Diffraction (XRD) analysis was performed using XPERT-PRO diffractometer (PANalytical BV the Netherlands). Fourier transform infrared (FT-IR) spectroscopy was carried out using Perkin Elmer Spectrum RX I FT-IR system in the 4000 – 500 cm⁻¹ range with a resolution of 2 cm⁻¹ to determine the sample surface functional groups. The FT-IR measurements were performed by properly blending the samples with KBr in a ratio of 1:100 and making them into transparent pellets before measurements. The Brunauer-Emmett-Teller (BET) technique was used to obtain the specific surface area and the N₂ adsorption/desorption isotherm measurements was performed at -196 °C with a Micrometrics TriStar II 3020. Raman analysis was performed using a Jobin-Yvon Horiba TX 64000 micro-spectrometer.

C. Electrochemical characterization

Three- and two-electrode measurements of the ACQS sample was performed in a multichannel VMP300 potentiostat/galvanostat (Biologic, France) workstation at room temperature. The electrodes for the three-electrode measurements were made by adding 80 wt.% ACQS material, 15 wt.% carbon black (to boost the conductivity of the material) and 5 wt.% polyvinylidene difluoride (PVdF) as a binder in an agate mortar and then mixed properly by adding 1-methyl-2-pyrrolidinone (NMP) drop-wise to make a paste. This was then pasted on nickel foam (NF)/carbon cloth current collectors and dried in an oven at 60 °C for several hours. The paste for the two-electrode tests was prepared using the same method but was coated on 16 mm diameter Nickel foam (NF) and dried at 60 °C, pressed and then assembled in a coin cell with a microfiber glass filter paper as a separator. The three electrode tests were performed in 3 M KNO₃, 6 M KOH and 1 M H₂SO₄ aqueous electrolytes using Ag/AgCl and glassy carbon as reference and counter electrodes respectively. The two electrode tests were then performed in 3 M KNO₃ neutral electrolyte because of the good reversibility of the material in both positive and negative voltage windows in this electrolyte. The specific capacitance, C_s for the half-cell electrode in a three electrode configuration is given by equation (1):²⁷

$$C_s(\text{F g}^{-1}) = \frac{I\Delta t}{m\Delta U} \quad (1)$$

The specific capacitance, C_{sp} per single electrode of the full device was calculated from the charge-discharge profile using equation (2):³

$$C_{sp}(\text{F g}^{-1}) = \frac{4I\Delta t}{m\Delta U} \quad (2)$$

Where *I* is the applied current (A), Δt is the discharge time (s), ΔU is the maximum cell voltage (V), and *m* is the total mass of the electrodes (g). Four (4) is a normalization factor of the symmetric electrodes to the mass of a single electrode. The energy density, *E_d* and power density, *P_d* were calculated from equation (3) and (4)^{3,28} (using parameters from equation (2)).

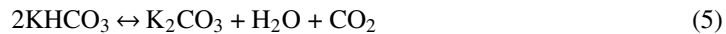
$$E_d(\text{W h kg}^{-1}) = \frac{C_{sp} \times \Delta U^2}{28.8} \quad (3)$$

$$P_d(\text{W kg}^{-1}) = \frac{E_d}{\Delta t} \quad (4)$$

III. RESULTS AND DISCUSSION

A. Material characterization

The SEM images of the ACQS material are presented in Fig. 1. Figs. 1(a) and (b) display the SEM images of the ACQS sample at low and high magnifications. The micrographs display 3D granular porous network structures of the material. The surface morphology of the material shows that KHCO_3 activation leads to the production of porous granular carbons which could improve the fast diffusion of ions along the material surfaces, useful for high-performance supercapacitor application.²³ The carbonization reaction mostly proceeds by the decomposition of KHCO_3 between the temperature ranges of 100 – 400 °C in the following reaction^{23,29,30}



K_2CO_3 decomposes into CO_2 and K_2O via a reaction with carbon to yield K at temperatures > 700 °C,



K_2CO_3 , however, does not melt at temperatures < 890 °C thereby allowing the granular morphology of the carbon to be preserved.²³ Any unreacted K_2CO_3 slowly decomposes at 850 °C according to the following equation:²³



At this temperature, the surface area and porosity of the material might be increased or modified because the CO_2 gas interacting with the carbon material to create more pores or modify existing ones.^{23,30}

The morphology of the as-synthesized ACQS material was further studied using HRTEM and is presented in Figs. 2(a) and (b). The high and low magnifications HRTEM images of the sample show no lattice fringes which are an indication that ACQS is mostly amorphous carbon. This is supported by the SAED pattern (inset to Fig. 2(b) which shows halo ring with no diffraction spots indicating the amorphicity of ACQS material.

EDX spectrum for the ACQS material is presented in Figure 2(c). The EDX plot confirmed the high carbon content of the as-synthesized ACQS material. The summary of the elemental composition is presented in Table I.

The oxygen content recorded is linked to the functional group present in the sample. The Cu recorded in trace amount was a contribution from the copper grid. The structure of the ACQS sample was studied by XRD technique. The XRD pattern of the ACQS sample (Fig. 3(a)) shows a wide and broad peak at 26° (002) and a weak peak at 51° (012). The diffraction peaks of the ACQS sample can be indexed to a hexagonal crystal structure of graphite having a space group of $P63mc$ utilizing the most appropriate matching Inorganic Crystal Structure Database (ICSD) card #31170. The peaks represent graphitic diffraction planes, but the broad and low intensity of the peaks is an indication that the ACQS material is mostly non-crystalline and can be referred to as amorphous carbon.³¹

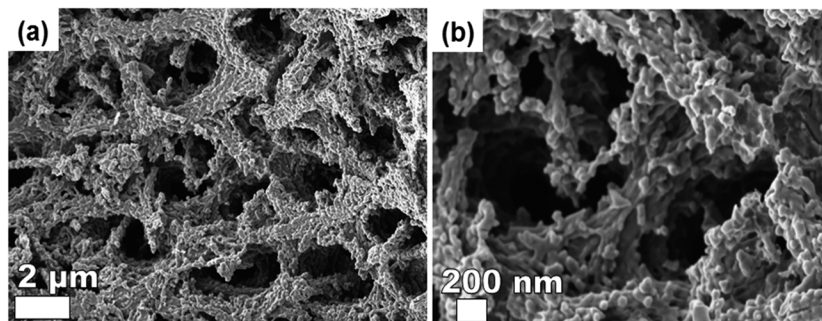


FIG. 1. SEM micrographs of ACQS at (a) low and (b) high magnification.

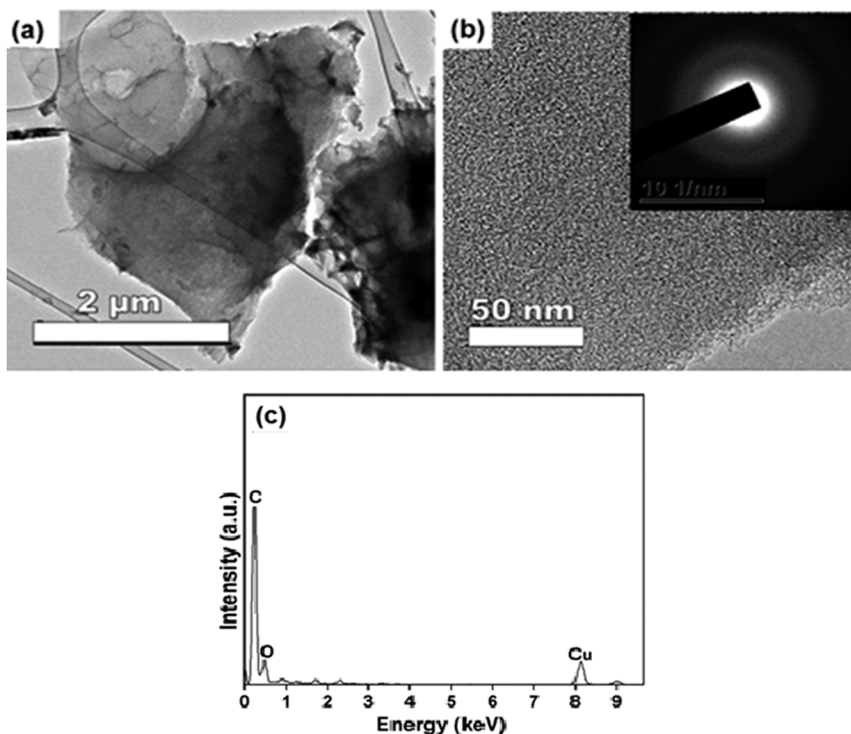


FIG. 2. HRTEM micrographs of ACQS at (a) low and (b) high magnifications; (c) EDX spectrum of ACQS.

FT-IR measurement was carried out to determine the presence of surface functional groups in the as-synthesized ACQS sample in the wavenumber range of 500 to 4000 cm^{-1} (Fig. 3(b)). The bands occurring at $\sim 3435 \text{ cm}^{-1}$ is as a result of the O-H stretching vibrations of water molecule due to surface hydroxyl groups. The peaks at $\sim 2942 \text{ cm}^{-1}$ indicate the C-H bond of the aliphatic group while the peak at $\sim 1608 \text{ cm}^{-1}$ is attributed to the C=O stretching vibrations of the carboxyl groups. The peaks occurring at $\sim 1050 \text{ cm}^{-1}$ and $\sim 582 \text{ cm}^{-1}$ may be due to the -C-C stretching vibration.^{3,32}

The ACQS sample composition was further analyzed with XPS. The high-resolution survey spectrum of the as-received ACQS sample (without sputter cleaning) is presented in Fig. 4(a) and a summary of the sample composition showing high carbon content of the as-synthesized ACQS material is displayed in Table II. Fig. 4(b) shows core level spectrum of C 1s with intensity peaks associated with the graphitic carbon C=C or C-C and other peaks relating to C-O, C-O=C or C=O. Figure 4c shows the spectrum for the O 1s with peaks at binding energies 531.7 eV and 533.2 eV associated with C-O and O-C indicating the presence of functional groups as suggested by FT-IR measurements.

The Raman spectrum of the ACQS sample is presented in Fig. 5(a). The spectrum shows the D band at $\sim 1338 \text{ cm}^{-1}$ and the G band at $\sim 1587 \text{ cm}^{-1}$ which are characteristic of disordered carbons in the sp^2 carbon network and graphitic carbon tangential vibrations respectively.^{33,34} The ratio of the intensity of the D and G peaks (I_D/I_G) expresses the extent of graphitization of the material. This ratio

TABLE I. Summary of the elemental composition of the sample.

| Element | Weight % | Atomic % |
|---------|----------|----------|
| C K | 89.24 | 91.75 |
| O K | 10.72 | 8.24 |
| Cu K | 0.05 | 0.01 |

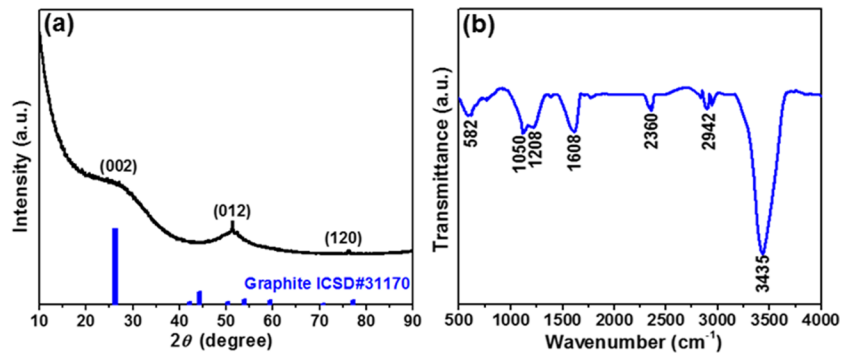


FIG. 3. (a) XRD spectrum (b) FT-IR spectrum of ACQS as-synthesized sample.

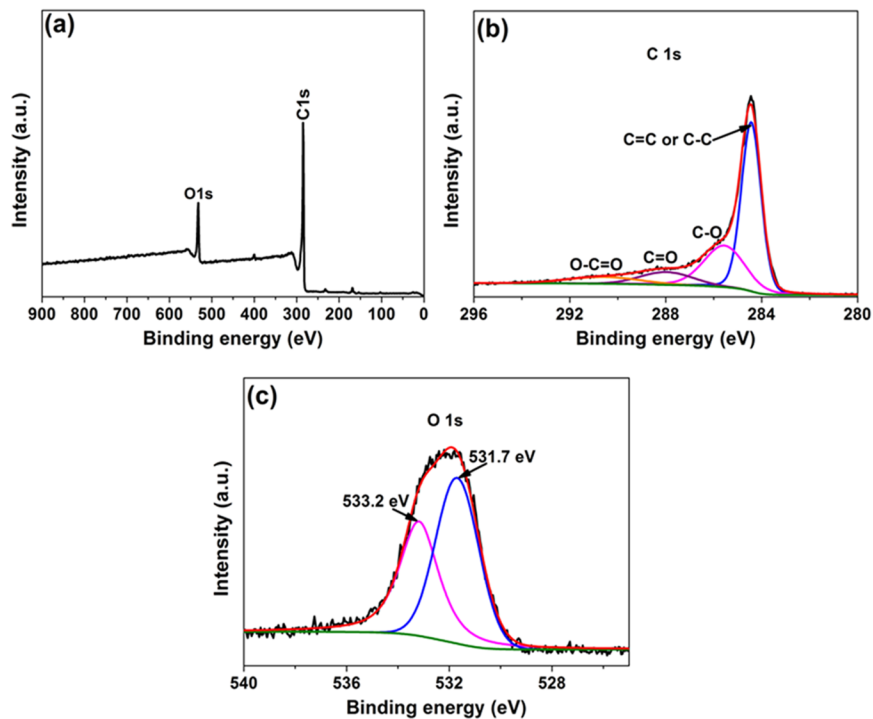


FIG. 4. (a) XPS survey spectrum of the as-received (without sputter cleaning) ACQS; High-resolution core level spectra of (b) C 1s and (c) O 1s of ACQS.

for the ACQS sample is 0.89 which is an indication of a low amount of graphitic crystallinity^{34–37} further confirming the observed XRD result. The broadband in Fig. 5(a) was deconvoluted using Lorentzian distribution for the curve fitting, (see Fig. 5(b)). The peak 1 curve is ascribed to the lattice vibrations linked to sp^2 - sp^3 network and peak 2 curve characteristically stems from the dissemination of unstructured carbon in interstitial sites in the disturbed graphitic lattice.³⁸ In a nutshell, the Raman spectrum indicates that the ACQS material contains a substantial quantity of interstitial unstructured carbon in the lattice framework.

TABLE II. A summary of the sample composition from XPS analysis.

| Sample | C at. % | O at. % |
|--------|--------------|--------------|
| ACQS | 88.92 ± 0.66 | 11.11 ± 0.29 |

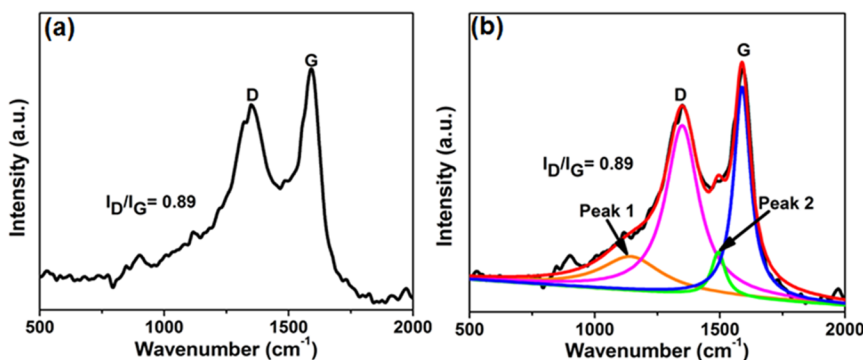


FIG. 5. (a) Raman spectra of ACQS and (b) Lorentzians curve fitting of the Raman spectrum for ACQS showing different peaks.

N₂ adsorption-desorption isotherms of the ACQS sample studied at -196 °C is presented in Fig. 6. Fig. 6 shows typical type IV with an H4 hysteresis loop signifying materials consisting of a microporous and mesoporous structure with relative pressure (P/P_0) > 0.2 and SSA of 1056.52 m² g⁻¹ and pore volume of 0.64 cm³ g⁻¹. The pore size distribution (PSD) (inset to Fig. 6 is in the range of 2-10 nm. The high SSA of the material and the PSD narrow range coupled with the granular microstructures can provide more active sites that ensure that the ACQS surface is sufficiently exposed for the electrolyte ions to access the micropores of the material.^{39,40}

B. Electrochemical analysis

The CV plots of the ACQS electrodes tested in the three-electrode configuration in 6 M KOH, 1 M H₂SO₄ and 3 M KNO₃ aqueous electrolytes at 50 mV s⁻¹ scan rate are shown in Fig. 7. Rectangular shaped CV profiles are observed for the ACQS sample in the positive and negative potential windows of 0.0 to 0.9 V and -0.9 to 0.0 V in 3 M KNO₃ aqueous neutral electrolyte, which are typical of electric double layer capacitive (EDLC) performance of the ACQS sample. It can be observed that the material is able to operate reversibly with typical rectangular EDLC curves and is stable within the positive and negative potential windows with di-hydrogen and oxygen evolutions only observed as the potential is increased to -1.0 and 1.0 V (See Fig. S1 in the [supplementary material](#)). From Fig. 7, quasi-rectangular curves can be observed for the ACQS sample in 6 M KOH in the negative potential window of -1.0 to 0.0 V and for the material tested in 1 M H₂SO₄ in the positive potential window of 0.0 to 0.9 V. Also for the ACQS sample tested in 6 M KOH, the onset of oxygen evolutions can already be observed beyond 0.2 V in the positive potential window and in 1 M H₂SO₄,

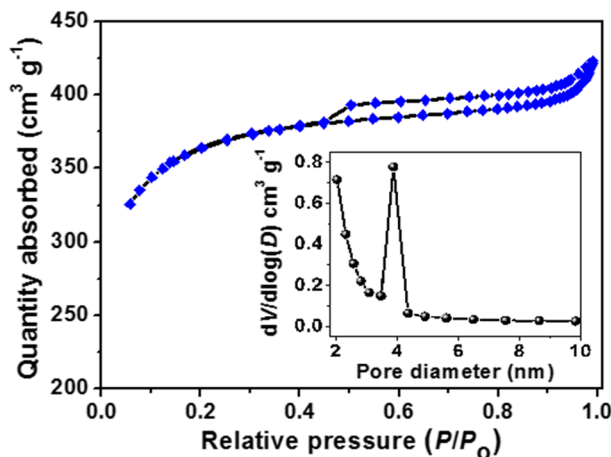


FIG. 6. Nitrogen adsorption-desorption isotherm with inset showing the BJH pore size distribution of ACQS.

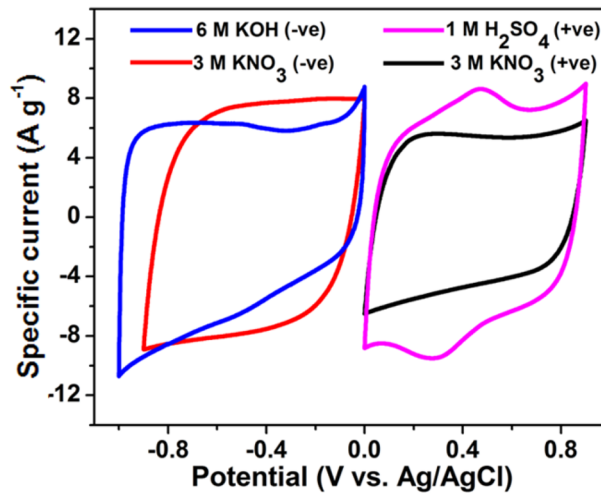


FIG. 7. CV curves at 50 mV s^{-1} scan rate in 3 M KNO_3 at -0.9 to 0.0 V and 0.0 to 0.9 V potential windows, 6 M KOH at -1.0 to 0.0 V potential window and 1 M H_2SO_4 at 0.0 to 0.9 V potential window.

oxygen evolutions can be observed as the potential approaches 1.0 V and di-hydrogen evolutions can be observed to already occur beyond -0.2 V (see Fig. S1 in the [supplementary material](#)). This phenomenon might be due to the decomposition of the ions of the electrolytes beyond 1.2 V and -1.2 V in the alkaline and acidic electrolytes respectively due to the thermal decomposition of water at 1.23 V.^{9,22,41} Also, from Fig. 7, the CV curves display different current responses within their respective operating potential windows (see the CV curves of the ACQS electrode materials at various scan rates ranging from 10 to 100 mV s^{-1} in 6 M KOH, 1 M H_2SO_4 and 3 M KNO_3 aqueous electrolytes in Fig. S2 of [supplementary material](#)). The disparity observed in electrochemical performances of the ACQS material in the various electrolytes could be due to the pH of the different electrolytes and/or pseudo-capacitance contribution from surface functional groups.^{26,42,43} For example, in 3 M KNO_3 neutral electrolyte, the H^+ and OH^- ions are fewer as compared to those in the acidic and alkaline electrolytes, and the pH is balanced on the H^+/OH^- ions such that the ions of the electrolyte are not biased to react with the electrode material in any preferred potential.^{3,26,44} Whereas the acidic and alkaline electrolytes have an abundance of the OH^- and H^+ ions which can make the material have a biased reaction in a given potential.⁴⁴ Other parameters such as the sizes of the ionic radii, ionic conductivities, and radii of the ionic hydration spheres and the mobility of the ions of the electrolytes may play a role as they interact with the electrode material.^{2,15,42,44} These electrolyte properties are itemized in Table III. From the Table III, it can be observed that the radius of hydration spheres for the electrolytes in any particular potential, decreases in this order: $\text{H}^+ < \text{K}^+ & \text{OH}^- < \text{NO}_3^- < \text{SO}_4^{2-}$ and the molar and ionic conductivities of the electrolyte ions increases in this order: $\text{H}^+ > \text{K}^+ & \text{OH}^- > \text{SO}_4^{2-} > \text{NO}_3^-$, so the molar and ionic conductivities might be a contributing factor in the difference in electrochemical responses. The high molar conductivities of the OH^- ions and the H^+ and SO_4^{2-} in KOH and H_2SO_4 electrolytes, which are higher than that of NO_3^- in KNO_3 might be the reason

TABLE III. Size, crystal radius, radius of hydration sphere, ionic conductivity, Gibbs energy and mobility of the electrolyte ions (These values were obtained from Refs. 2 and 43).

| Ion | Crystal radius (Å) | Hydration sphere radius (Å) | Molar conductivity ($\text{S cm}^2 \text{ mol}^{-1}$) | Ionic mobility ($\mu\text{10}^{-5} \text{ cm}^2 \text{ s}^{-1} \text{ V}^{-1}$) |
|--------------------|--------------------|-----------------------------|---|---|
| K^+ | 1.33 | 3.31 | 73.5 | 7.6 |
| H^+ | 1.15 | 2.80 | 349.8 | 36.2 |
| SO_4^{2-} | 2.90 | 3.79 | 160.0 | 8.3 |
| NO_3^- | 2.64 | 3.35 | 71.42 | - |
| OH^- | 1.76 | 3.00 | 198.0 | 20.6 |

for the higher specific capacitance of the material in the H_2SO_4 and KOH electrolytes. However, the ACQS material is only able to operate reversibly in the positive and negative potential windows in the 3 M KNO_3 electrolyte, hence its utilization in the symmetric device fabrication.

The Charge-discharge (CD) curves measured in the positive and negative potential windows of 0.0 to 0.9 V and -0.9 to 0.0 V, respectively in 3 M KNO_3 at 1.0 A g^{-1} to 5.0 A g^{-1} specific current are presented in Figs. 8(a) and (b). The CD profiles show triangular symmetrical shapes corresponding to the characteristic EDLC behavior observed for the CV curves.

The Specific capacitance (C_S) values calculated from the CD profiles in the positive potential window are from 133 to 94.0 F g^{-1} and in the negative potential window, from 167 to 139 F g^{-1} , at 1.0 to 5.0 A g^{-1} , respectively. The CD profiles for the test performed at specific currents of 1.0 to 5.0 A g^{-1} in 6 M KOH in the negative potential window of -1.0 to 0.0 V and in 1 M H_2SO_4 positive potential window of 0.0 to 0.9 V are presented in Figs. 8(c) and (d). The observed triangular shapes are however slightly distorted due to the presence of hydroxyl functional groups in the sample (as indicated by FT-IR measurement), which could readily react with the abundant H^+ and OH^- ions. The calculated C_S values from the CD profiles for the material in 6 M KOH are from 250 to 130 F g^{-1}

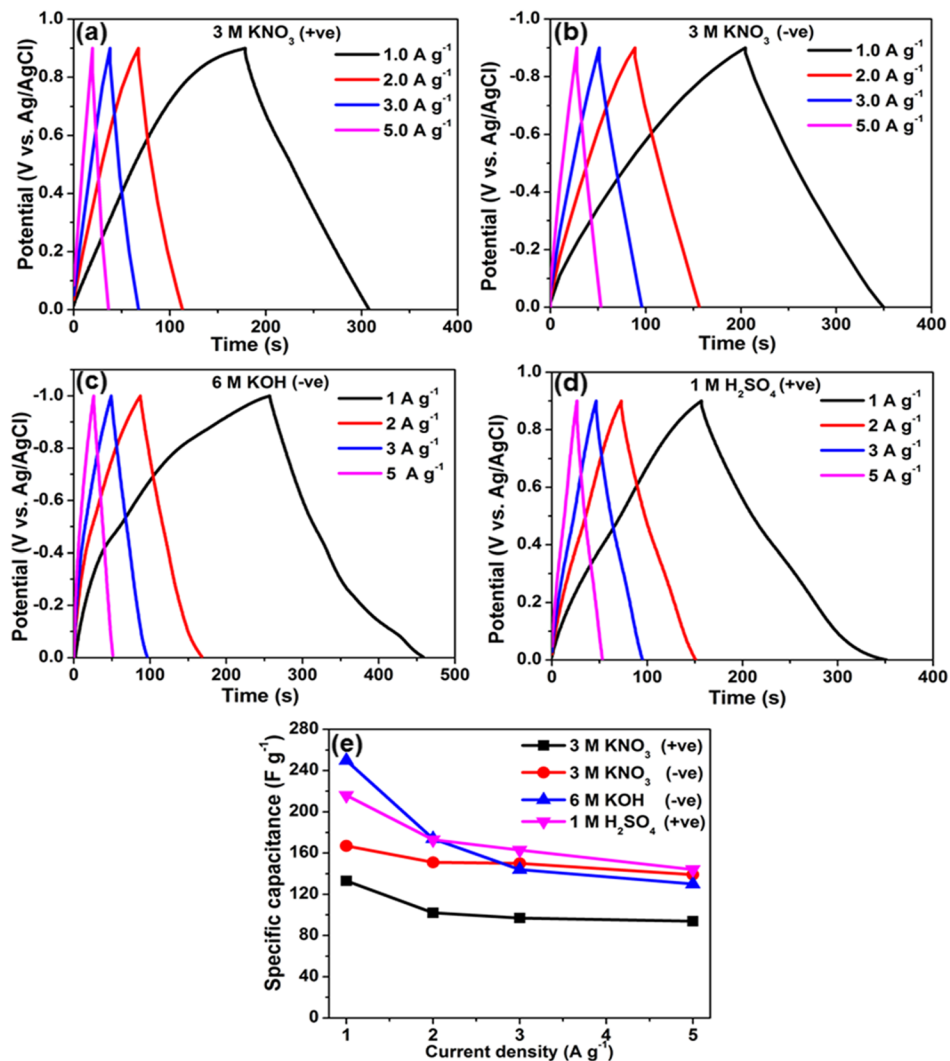


FIG. 8. Charge-discharge profile at 1.0 A g^{-1} to 5.0 A g^{-1} specific currents for the ACQS material in (a) and (b) 3 M KNO_3 in the positive and negative potential windows of 0.0 to 0.9 V and -0.9 to 0.0 V, (c) 6 M KOH in the negative potential window of -1.0 to 0.0 V and (d) 1 M H_2SO_4 in the positive potential window of 0.0 to 1.0 V. (e) Specific capacitance versus specific current in 3 M KNO_3 , 6 M KOH and 1 M H_2SO_4 in the positive and negative potential windows.

and the C_S values calculated from the CD profiles for the material in 1 M H_2SO_4 are from 216 to 144 $F g^{-1}$ at 1.0 to 5.0 $A g^{-1}$, respectively. A plot of the C_S values as a function of specific currents for the material in 3 M KNO_3 , 6 M KOH and 1 M H_2SO_4 electrolytes in the positive and negative potential windows are shown in Fig. 8(e).

A symmetric device was assembled based on the performance of the material in the three-electrode configuration. The CV plots of the the ACQS//ACQS symmetric device fabricated from ACQS electrodes in 3 M KNO_3 at various voltage windows ranging from 1.4 to 1.8 V at 25 $mV s^{-1}$ scan rate is presented in Fig. 9(a). The optimization of the working voltage windows is to obtain the most stable voltage window of the symmetric device. It has been shown in previous reports that neutral electrolytes are able to function with large operating potentials as a result of high over potential for di-hydrogen evolutions.^{7,9,26,44}

The CV curves displayed rectangular shapes within the operating voltages but a current leap begins to be observed as the voltage is increased to 1.8 V. This anodic current leap towards the more positive voltage might be as a result of oxygen or gas exudation as the voltage reaches 1.8 V.⁴⁵ However functional groups present in the sample can enhance the ion diffusion culminating in active electron mobility in the granular porous carbon sample. Hence, the working voltage of 1.8 V is stable for the symmetric device.

Fig. 9(b) shows the CV plots of the symmetric device in the voltage window of 0 - 1.8 V at scan rates of 10 to 100 $mV s^{-1}$. The CV curves maintain symmetric rectangular shapes as the scan rate increases up to 2.0 $V s^{-1}$ as shown in Fig. 9(c). This is an indication of a highly capacitive electrochemical performance of the ACQS material.^{14,45}

The CD profiles recorded within the voltage window of 0.0 – 1.8 V at varying specific currents of 0.5 $A g^{-1}$ to 5.0 $A g^{-1}$ are presented in Fig. 9(d). Linear CD profiles are observed which corresponds to typical EDLC behavior showing high reversibility of anodic and cathodic ionic transport.

The plot of the C_{sp} values calculated from the CD profiles versus specific currents for the ACQS//ACQS symmetric device is shown in Fig. 10(a). A C_{sp} value of 122 $F g^{-1}$ is recorded for the

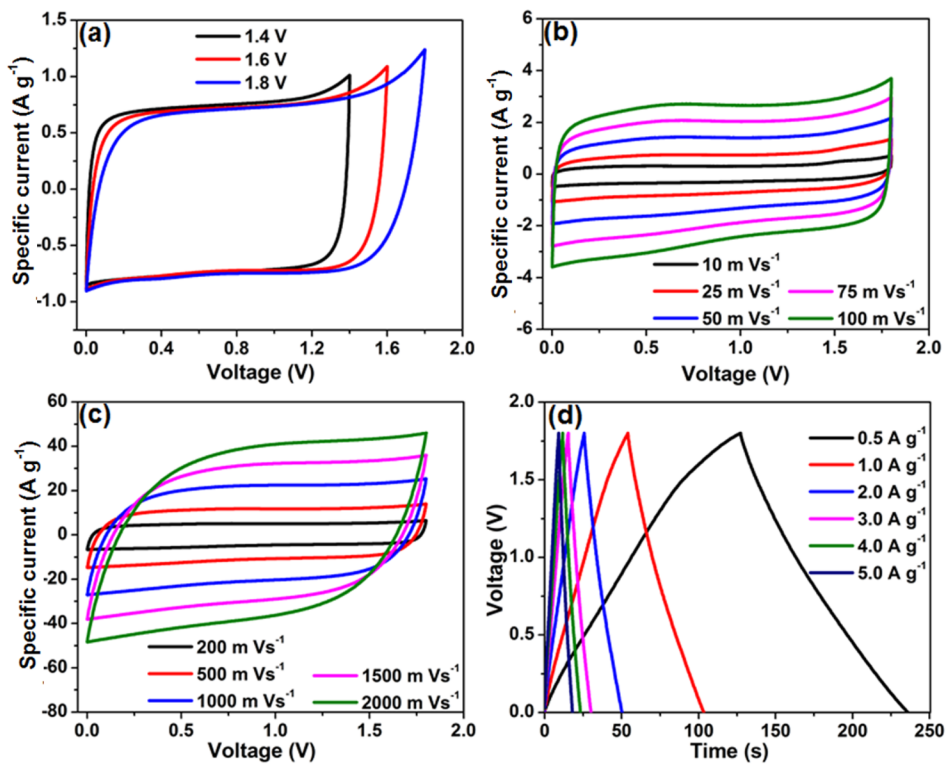


FIG. 9. (a) CV plots at varied operating voltage windows (b) and (c) detailed CV plots at various scan rates (d) associated CD profiles for the of ACQS//ACQS symmetric device in 3 M KNO_3 .

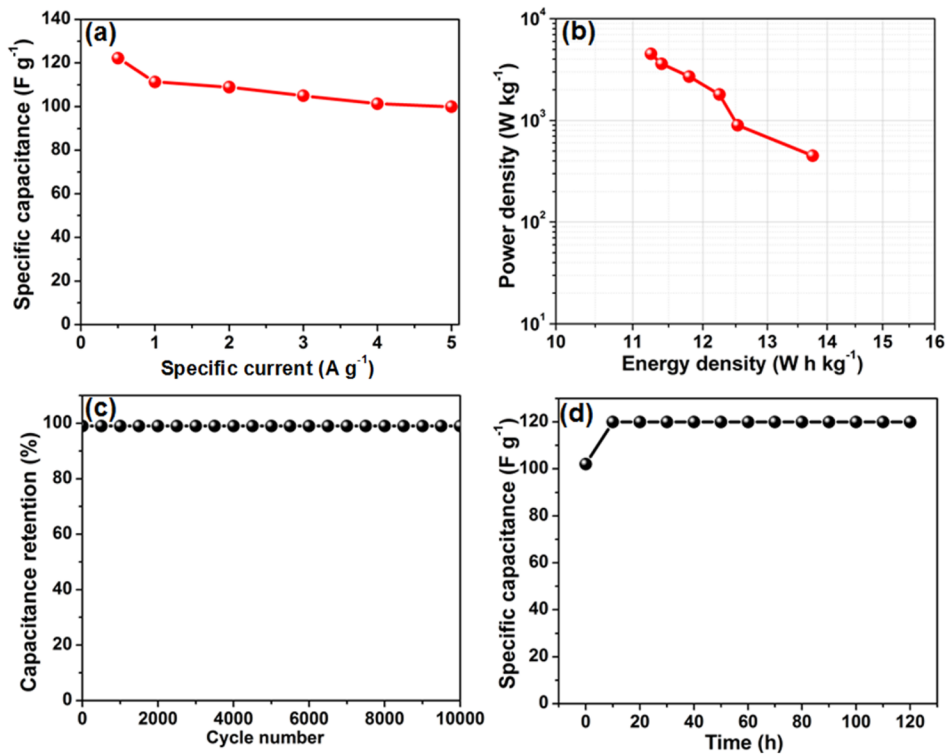


FIG. 10. (a) Specific capacitance versus specific current (b) Ragone Plot (c) Stability plot: capacitance retention versus cycle number at 5.0 A g^{-1} (d) Specific capacitance versus floating time for the ACQS//ACQS symmetric device.

electrode at 0.5 A g^{-1} and 100 F g^{-1} at 5.0 A g^{-1} . A good rate capability is observed for the symmetric device as it displays more than 90% capacitance retention for each increase in specific current. This shows the ability of the material to retain reasonable capacitance even at high specific current. A plot of energy density versus power density (Ragone plot) for the symmetric device is shown in Fig. 10(b). The device displays an energy density of $\sim 14 \text{ W h kg}^{-1}$ and power density of $\sim 450 \text{ W kg}^{-1}$ at a specific current of 0.5 A g^{-1} (as determined from equation 3 and 4). This work displays remarkable electrochemical performance relative to other biomass-derived activated carbon.^{6,18,46–50} A correlation of this results with other earlier reports from biomass-derived activated carbon (AC), which was activated with KOH, ZnCl_2 and MgO, is shown in Table IV. The high electrochemical performance of this device might be as result of the high SSA, high pore volume and large mesopore volume which resonate well with the granular porous network and good pore size distribution with good packing properties which enhance proper ion transfer.^{1,18,51} The stability of the symmetric

TABLE IV. Comparison of electrochemical performance of different materials with present work.

| Precursor | Activation agent | S_{BET} ($\text{m}^2 \text{ g}^{-1}$) | Voltage (V) | Specific capacitance (F g^{-1}) | Specific Current (A g^{-1}) | Electrolyte | Energy Density (W h Kg^{-1}) | Ref |
|-----------------------------|-----------------------------------|--|-------------|--|--|--------------------------------------|---|------------------|
| Hazel nutshell | MgO | 552 | 2.0 | 19.9 | 0.25 | 1 M Na_2SO_4 | 11.1 | 50 |
| Coconut shell | KOH | 1416 | 1.3 | 186 | 0.25 | Polymer Gel | 11 | 49 |
| Cork | KOH | 1081 | 1.8 | 166 | 0.5 | 1 M Na_2SO_4 | 18.6 | 9 |
| Cotton Fiber | ZnCl_2 | 2549 | 1.8 | 239 | 0.5 | 1 M Na_2SO_4 | 13.75 | 47 |
| Coconut shell | ZnCl_2 | 2440 | - | - | - | H_2SO_4 | 7.6 | 18 |
| Pistachio nutshells | KOH | 1069 | 1.1 | 261 | 0.2 | 6 M KOH | 10 | 46 |
| Cork (Quercus Suber) | KHCO_3 | 1056 | 1.8 | 122.2 | 0.5 | 3 M KNO_3 | 14.0 | This work |

device studied at 5.0 A g^{-1} and 1.8 V maximum cell working voltage over 10,000 constant charge-discharge cycles is presented in Fig. 10(c). The device displayed $\sim 100\%$ capacitance retention after the 10,000th charge-discharge cycle with no degradation observed in the cell performance. The device was subsequently subjected to a voltage holding test to further investigate the long-term stability of the cell. Voltage holding as compared to the normal charging and discharging over many cycles helps to study the cell stability and shows the real resistance effects and physiochemical deterioration that might be taking place during the electrochemical process⁴¹ after floating at 1.8 V maximum voltage. The voltage holding plot which is a plot of specific capacitance as a function of voltage holding time is presented in Fig. 10(d). The floating process involves periodic potentiostatic mode and subsequent galvanostatic charge-discharge cycle at 1.0 A g^{-1} . The floating and charge-discharge cycles are iterated for a period of 120 h. The voltage holding analysis showed an improvement in the performance of the device which increases after the first 10 h of floating which is an indication that more pore sites were accessed by the electrolyte as a result of prolonged floating, with only slight decay at the end of 120 h. The increase in capacitance might also be due to the expansion of the material granular porous network thereby allowing more adsorption and intercalation of ions into the material active sites thus increasing the cell capacitance.^{35,52}

The electrochemical impedance spectroscopy (EIS) measurements were carried out in an open circuit potential and the Nyquist plots for the ACQS//ACQS symmetric device before and after stability is presented in Fig. 11(a). The EIS study is important for understanding the electron and ion transport in the electrolyte and the electrode material.²¹ The EIS study was performed in an open circuit potential from 0.01 Hz to 100 kHz frequencies. Nearly vertical lines and small semi-circles (inset to Fig. 11(a)) can be observed at the high and low-frequency regions of the Nyquist plots indicating the presence of charge transfer resistance R_{ct} of 0.2Ω showing good electron and ion conductivity and typical electric double layer capacitive behavior. R_{ct} of 0.5Ω was obtained after cycling stability test, this large increase of the R_{ct} value after stability could be attributed to

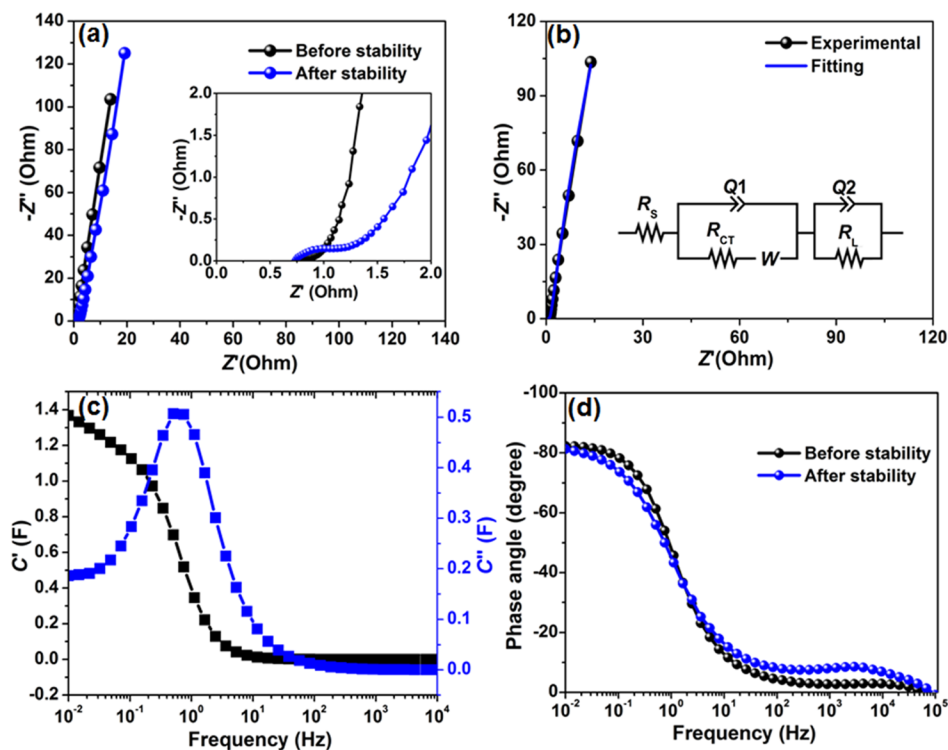


FIG. 11. (a) EIS plot before and after cycling test (b) EIS plots on open circuit potential and equivalent circuit (inset to the figure) (c) Real and imaginary parts of the cell capacitance versus frequency and (d) Phase angle as a function of frequency before and after stability, for the ACQS//ACQS cell in 3 M KNO_3 .

the fact that electron transfer and ion diffusion within the electrode material/electrolyte has slowed down as a result of the prolonged cycling of the electrode.⁴⁰ The intersection of the semicircle with the Z' axis shows the solution resistance (R_s) before and after cycling stability, with values of 0.75 Ω and 0.74 Ω respectively. This R_s element is made up of the electrolytic resistance, intrinsic electrode material resistance and the resistance between the electrode material and the current collector.^{35,53}

The equivalent series circuit fitted for the Nyquist plot before stability is as presented in Fig. 11(b). The equivalent series circuit shows a series connection between the solution resistance, R_s and the constant phase element, Q_1 which is connected in parallel with R_{ct} , the charge transfer resistance. The Q_1 element shows the double layer capacitance associated with the Warburg diffusion element (W) which is connected in series with R_{ct} . Q_2 is the mass capacitance and is associated with the ideal polarizable capacitance connected in parallel to an impedance characteristic element R_L , which accounts for the shifting of the vertical line from the typical EDLC characteristic.^{54,55} The deviation from the typical vertical behavior connotes that there is a leakage resistance, R_L which is a resistive element connected with Q_2 .

The impedance (Z) of Q_1 , is expressed as;^{55,56}

$$Z_{Q_1} = e(j\omega)^{-b} \quad (8)$$

Where e and b are frequency-independent constants and ω is angular frequency. $C'(\omega)$ and $C''(\omega)$ which are the real and imaginary parts of the capacitance versus frequency is presented in Fig. 11(c). A value of 1.38 F was recorded for C' at a frequency of 10 mHz is which is the real attainable capacitance of this symmetric device at this frequency. C'' describes the frequency transition between a typical capacitive and resistive characteristics of the symmetric cell⁵⁷ with a relaxation time (τ) of 1.32 s corresponding to a frequency of ~ 1.0 Hz which was calculated for the symmetric cell using the equation:

$$\tau = \frac{1}{f_{max}} = 2\pi\omega_{max}^{-1} \quad (9)$$

The relaxation time simply means that the stored energy contained in the ACQS//ACQS symmetric cell can be retrieved in a period of 1.32 s. The phase angle of the cell versus frequency is presented in Fig. 11(d). The phase angle of the cell is recorded at approximately -83° (which is close to -90°) and a value of -81° was recorded for the phase angle after cycling stability, which is indicative of the good capacitive performance of the symmetric cell similar to the ideal device.

IV. CONCLUSIONS

Activated carbon derived from cork (*Quercus Suber*) (ACQS) was successfully produced via a two-step environment-friendly synthesis route. This green synthesis route makes the synthesized material less toxic for utilization as an electrode material for energy storage application. The activated carbon has well-defined microporous and mesoporous structures which provide a good interface for fast rate ion transfer. The granular network structures also provide good packing properties for better ion diffusion and intercalation. The electrochemical study of the symmetric device assembled from the synthesized activated carbon as electrode materials displayed a specific capacitance of 122.2 F g⁻¹, energy density of ~ 14.0 Wh Kg⁻¹ and power density of 450.0 W kg⁻¹ at a current density of 0.5 A g⁻¹ with an excellent long-term cycling life after 10,000 CD cycles and subsequent floating at maximum voltage for 120 h. The excellent stability after floating test and the $\sim 100\%$ capacitance retention after 10000 CD cycles makes the Cork derived activated carbon material a potential material for energy storage application.

SUPPLEMENTARY MATERIAL

See [supplementary material](#) for additional information on the electrochemical characterization of the ACQS material.

ACKNOWLEDGMENTS

The South African Research Chairs Initiative (SARChI) of the Department of Science and Technology, the National Research Foundation (NRF) of South Africa (Grant No. 61056) through SARChI, and the Department of physics, University of Pretoria is acknowledged for their financial support. Any view, result and conclusion or recommendation expressed in this work is that of the author(s) and the NRF does not accept any liability in this regard. Mr. J. Lekitima is acknowledged for the FT-IR measurements.

- ¹ J. Wang and S. Kaskel, *J. Mater. Chem.* **22**, 23710 (2012).
- ² C. Zhong, Y. Deng, W. Hu, J. Qiao, L. Zhang, and J. Zhang, *Chem. Soc. Rev.* **44**, 7484 (2015).
- ³ A. Bello, N. Manyala, F. Barzegar, A. A. Khaleed, D. Y. Momodu, and J. K. Dangbegnon, *RSC Adv.* **6**, 1800 (2016).
- ⁴ R. Li, S. Wang, Z. Huang, F. Lu, and T. He, *J. Power Sources* **312**, 156 (2016).
- ⁵ H. Sun, L. Cao, and L. Lu, *Energy Environ. Sci.* **5**, 6206 (2012).
- ⁶ X. Li, W. Xing, S. Zhuo, J. Zhou, F. Li, S.-Z. Qiao, and G.-Q. Lu, *Bioresour. Technol.* **102**, 1118 (2011).
- ⁷ Z.-Z. Pan, L. Dong, W. Lv, D. Zheng, Z. Li, C. Luo, C. Zheng, Q.-H. Yang, and F. Kang, *Chem. An Asian J.* **12**, 503 (2017).
- ⁸ P. Simon and Y. Gogotsi, *Acc. Chem. Res.* **46**, 1094 (2013).
- ⁹ F. O. Ochai-Ejeh, A. Bello, J. Dangbegnon, A. A. Khaleed, M. J. Madito, F. Bazegar, and N. Manyala, *J. Mater. Sci.* **52**, 10600 (2017).
- ¹⁰ P. Simon and Y. Gogotsi, *Nat. Mater.* **7**, 845 (2008).
- ¹¹ J. Pu, F. Cui, S. Chu, T. Wang, E. Sheng, and Z. Wang, *ACS Sustain. Chem. Eng.* **2**, 809 (2014).
- ¹² H. Jiang, P. S. Lee, and C. Li, *Energy Environ. Sci.* **6**, 41 (2013).
- ¹³ J. R. Miller and P. Simon, *Science* **321**, 651 (2008).
- ¹⁴ Y. Jang, J. Jo, Y.-M. Choi, I. Kim, S.-H. Lee, D. Kim, and S. M. Yoon, *Electrochim. Acta* **102**, 240 (2013).
- ¹⁵ R. N. Reddy and R. G. Reddy, *J. Power Sources* **124**, 330 (2003).
- ¹⁶ L. Dong, C. Xu, Q. Yang, J. Fang, Y. Li, and F. Kang, *J. Mater. Chem. A* **3**, 4729 (2015).
- ¹⁷ L. Dong, C. Xu, Y. Li, Z.-H. Huang, F. Kang, Q.-H. Yang, and X. Zhao, *J. Mater. Chem. A* **4**, 4659 (2016).
- ¹⁸ A. Jain, C. Xu, S. Jayaraman, R. Balasubramanian, J. Y. Lee, and M. P. Srinivasan, *Microporous Mesoporous Mater.* **218**, 55 (2015).
- ¹⁹ A. Jain, R. Balasubramanian, and M. P. Srinivasan, *Chem. Eng. J.* **283**, 789 (2016).
- ²⁰ W. Gu and G. Yushin (2013).
- ²¹ B. Abdulhakeem, B. Farshad, M. Damilola, T. Fatemeh, F. Mopeli, D. Julien, and M. Ncholu, *RSC Adv.* **4**, 39066 (2014).
- ²² F. Béguin, V. Presser, A. Balducci, and E. Frackowiak, *Adv. Mater.* **26**, 2219 (2014).
- ²³ M. Sevilla and A. B. Fuertes, *ChemSusChem* **9**, 1880 (2016).
- ²⁴ R. C. Saxena, D. K. Adhikari, and H. B. Goyal, *Renew. Sustain. Energy Rev.* **13**, 167 (2009).
- ²⁵ H. B. Goyal, D. Seal, and R. C. Saxena, *Renew. Sustain. Energy Rev.* **12**, 504 (2008).
- ²⁶ L. Demarconnay, E. Raymundo-Piñero, and F. Béguin, *Electrochem. Commun.* **12**, 1275 (2010).
- ²⁷ S. Ratha, S. R. Marri, N. A. Lanzillo, S. Moshkalev, S. K. Nayak, J. N. Behera, and C. S. Rout, *J. Mater. Chem. A* **3**, 18874 (2015).
- ²⁸ G. Yu, L. Hu, M. Vosgueritchian, H. Wang, X. Xie, J. R. McDonough, X. Cui, Y. Cui, and Z. Bao, *Nano Lett.* **11**, 2905 (2011).
- ²⁹ J. Przepiorski and A. Oya, *J. Mater. Sci. Lett.* **17**, 679 (1998).
- ³⁰ J. Hayashi, T. Horikawa, I. Takeda, K. Muroyama, and F. Nasir Ani, *Carbon* **40**, 2381 (2002).
- ³¹ X. Zhang, W. Lv, Y. Tao, J. Shao, J. Shao, C. Zhang, D. Liu, J. Luo, D.-W. Wang, and Q.-H. Yang, *Chem. Mater.* **26**, 6896 (2014).
- ³² A. E. Ofomaja and E. B. Naidoo, *Chem. Eng. J.* **175**, 260 (2011).
- ³³ J. W. Lee, A. S. Hall, J.-D. Kim, and T. E. Mallouk, *Chem. Mater.* **24**, 1158 (2012).
- ³⁴ J. K. Gan, Y. S. Lim, A. Pandikumar, N. M. Huang, and H. N. Lim, *RSC Adv.* **5**, 12692 (2015).
- ³⁵ N. Manyala, A. Bello, F. Barzegar, A. A. Khaleed, D. Y. Momodu, and J. K. Dangbegnon, *Mater. Chem. Phys.* **182**, 139 (2015).
- ³⁶ D. S. Patil, J. S. Shaikh, D. S. Dalavi, S. S. Kalagi, and P. S. Patil, *Mater. Chem. Phys.* **128**, 449 (2011).
- ³⁷ M. D. Stoller and R. S. Ruoff, *Energy Environ. Sci.* **3**, 1294 (2010).
- ³⁸ A. Sadezky, H. Muckenhuber, H. Grothe, R. Niessner, and U. Pöschl, *Carbon* **43**, 1731 (2005).
- ³⁹ A. G. Pandolfo and A. F. Hollenkamp, *J. Power Sources* **157**, 11 (2006).
- ⁴⁰ L. Dong, G. Liang, C. Xu, D. Ren, J. Wang, Z.-Z. Pan, B. Li, F. Kang, and Q.-H. Yang, *J. Mater. Chem. A* **5**, 19934 (2017).
- ⁴¹ A. Bello, F. Barzegar, M. J. Madito, D. Y. Momodu, A. A. Khaleed, T. M. Masikhwa, J. K. Dangbegnon, and N. Manyala, *Electrochim. Acta* **213**, 107 (2016).
- ⁴² X. Zhang, X. Wang, L. Jiang, H. Wu, C. Wu, and J. Su, *J. Power Sources* **216**, 290 (2012).
- ⁴³ L. Qie, W. Chen, H. Xu, X. Xiong, Y. Jiang, F. Zou, X. Hu, Y. Xin, Z. Zhang, and Y. Huang, *Energy Environ. Sci.* **6**, 2497 (2013).
- ⁴⁴ K. Fic, G. Lota, M. Meller, and E. Frackowiak, *Energy Environ. Sci.* **5**, 5842 (2012).
- ⁴⁵ J. H. Chae and G. Z. Chen, *Electrochim. Acta* **86**, 248 (2012).
- ⁴⁶ J. Xu, Q. Gao, Y. Zhang, Y. Tan, W. Tian, L. Zhu, and L. Jiang, *Sci. Rep.* **4**, 845 (2014).
- ⁴⁷ G. Ma, D. Guo, K. Sun, H. Peng, Q. Yang, X. Zhou, X. Zhao, and Z. Lei, *RSC Adv.* **5**, 64704 (2015).
- ⁴⁸ D. Momodu, M. Madito, F. Barzegar, A. Bello, A. Khaleed, O. Olaniyan, J. Dangbegnon, and N. Manyala, *J. Solid State Electrochem.* **21**, 859–872 (2017).
- ⁴⁹ F. Barzegar, A. A. Khaleed, F. U. Ugbo, K. O. Oyeniran, D. Y. Momodu, A. Bello, J. K. Dangbegnon, and N. Manyala, *AIP Advances* **6**, 115306 (2016).

- ⁵⁰ N. Sinan and E. Unur, *J. Energy Chem.* **26**, 783 (2017).
- ⁵¹ F. Barzegar, A. Bello, O. O. Fashedemi, J. K. Dangbegnon, D. Y. Momodu, F. Taghizadeh, and N. Manyala, *Electrochim. Acta* **180**, 442 (2015).
- ⁵² G. Ren, X. Pan, S. Bayne, and Z. Fan, *Carbon* **71**, 94 (2014).
- ⁵³ J. Luo, H. D. Jang, and J. Huang, *ACS Nano* **7**, 1464 (2013).
- ⁵⁴ H. Wang, Y. Liang, T. Mirfakhrai, Z. Chen, H. Sanchez Casalongue, and H. Dai, *Nano Res.* **4**, 729 (2011).
- ⁵⁵ F. Barzegar, A. Bello, D. Y. Momodu, J. K. Dangbegnon, F. Taghizadeh, M. J. Madito, T. M. Masikhwa, and N. Manyala, *RSC Adv.* **5**, 37462 (2015).
- ⁵⁶ D. Pech, M. Brunet, H. Durou, P. Huang, V. Mochalin, Y. Gogotsi, P.-L. Taberna, and P. Simon, *Nat. Nanotechnol.* **5**, 651 (2010).
- ⁵⁷ P. L. Taberna, P. Simon, and J. F. Fauvarque, *J. Electrochem. Soc.* **150**, A292 (2003).